Chapter 1
Self-organized Surface Patterns Originating from Laser-Induced Instability

Olga Varlamova, Juergen Reif, Sergey Varlamov and Michael Bestehorn

Abstract Self-organized surface pattern formation upon femtosecond laser ablation is considered in framework of an adopted surface erosion model, based on the description for spontaneous pattern formation on ion bombarded surfaces. We exploit the similarity to ion-beam sputtering and extend a corresponding model for laser ablation by including laser polarization. We find that an asymmetry in deposition and dissipation of incident laser energy, related to the laser polarization, results in a corresponding dependence of coefficients in a nonlinear equation of the Kuramoto-Sivashinsky type. We present the surface morphologies obtained by this model for different polarization of the laser beam and discuss a time evolution of the nanopattern. A comparison of numerical results with experimental data shows an excellent qualitative agreement. Our results support the non-linear self-organization mechanism of pattern formation on the surface of solids.

O. Varlamova (✉) · J. Reif
LS Experimentalphysik II, Brandenburg University of Technology (BTU) Cottbus,
Platz der Deutschen Einheit 1, 03046 Cottbus, Germany
e-mail: olga.varlamova@tu-cottbus.de

J. Reif
e-mail: reif@tu-cottbus.de

S. Varlamov · M. Bestehorn
LS Theoretische Physik II, Brandenburg University of Technology (BTU) Cottbus,
Platz der Deutschen Einheit 1, 03046 Cottbus, Germany
e-mail: sergev@physik.tu-cottbus.de

M. Bestehorn
e-mail: bes@physik.tu-cottbus.de

S. Sakabe et al. (eds.), *Progress in Nonlinear Nano-Optics*,
Nano-Optics and Nanophotonics, DOI 10.1007/978-3-319-12217-5_1

1.1 Self-organized Laser-Induced Surface Structures

1.1.1 Experimental Observations

The development of laser technologies and application of ultrashort, i.e. subpicosecond pulses in material processing, has revealed a large diversity of surface structures distinct from earlier observed LIPSS [1–4]. Along with the classical ripples with periods of about the laser wavelength, also fine nano-ripples with a feature size much smaller than the applied laser wavelength and coarse macro-ripples with a lateral size in a several microns range, as well as even more complex patterns like arrays of conical features were registered at the laser-modified area [5–21]. Very often, several different types of these structures can coexist in the same ablation spot.

Since the end of the 1990s it has been established that, typically, these structures can be generated upon irradiation of the picosecond to femtosecond range at intensities below or about the single-shot ablation threshold on surfaces of different solids (crystalline and amorphous insulators, semiconductors, and metals). The laser-induced morphology is qualitatively independent of the kind of ablated material and of their crystallographic structure. Generally, the LIPSS completely develop only after a considerable number of pulses [7, 9, 10], and positive feedback plays an important role in the ripple formation process [17, 22, 23]. The ripples period and complexity vary across the ablation spot, from fine and regular at the edge to coarse and complex in the middle, depending rather on the local pulse intensity than on the laser wavelength [10].

Pattern morphology and orientation are, typically, controlled by the polarization state of the laser electric field [24–27]. Linear high-periodic structures with multiple bifurcations or an arrangement of nanospheres are typical for linearly and circularly polarized light, respectively, as shown in Fig. 1.1a, b; a mixture of long and short

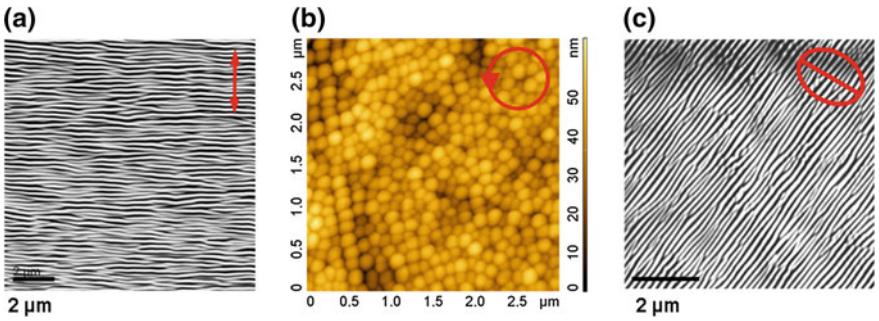

Fig. 1.1 Micrographs of sections from the *bottom* of ablation craters obtained on a CaF_2 surface. **a**, **b** and **c** show patterns generated with *linearly*, *circularly* and *elliptically* polarized irradiation (λ_{laser} = 800 nm, τ_{pulse} = 120 fs), respectively (5,000 pulses@8.1 TW/cm^2) (State of the laser polarization indicated at the *right upper corner*)

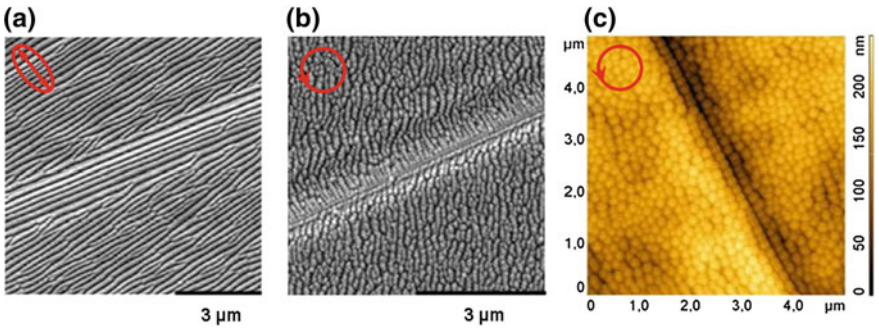

Fig. 1.2 Influence of extended surface defects (scratches, cleavage steps) on the orientation of nanostructures: **a** CaF_2 (111) irradiated with 5,000 pulses of *elliptically* polarized light at laser intensity 8.3 TW/cm^2; **b** CaF_2 (111) irradiated with 120,000 pulses of *circularly* polarized light at laser intensity 1.9 TW/cm^2; **c** NaCl (111) irradiated with 5,000 pulses of *circularly* polarized light at intensity 7.9 TW/cm^2

lines (Fig. 1.1c) is observed for elliptically polarized pulses. However, also extended macroscopic surface defects play an important role as an order parameter [28], the influence of surface defects on structure orientation is even significantly stronger than that of the polarization (Fig. 1.2).

At an increasing irradiation dose, also the superposition of several structures can be observed. Detailed inspection of the ablation spot on CaF_2, induced upon 10,000 pulses of linear polarization at intensity 8.4 TW/cm^2, reveals complex structuring of the crater walls. A coarse overstructure that is not really related to the polarization direction (Fig. 1.3a), and fine ripples with spacing less than 20 nm, directed perpendicular to the laser electric field (Fig. 1.3b), coexist in the irradiated area.

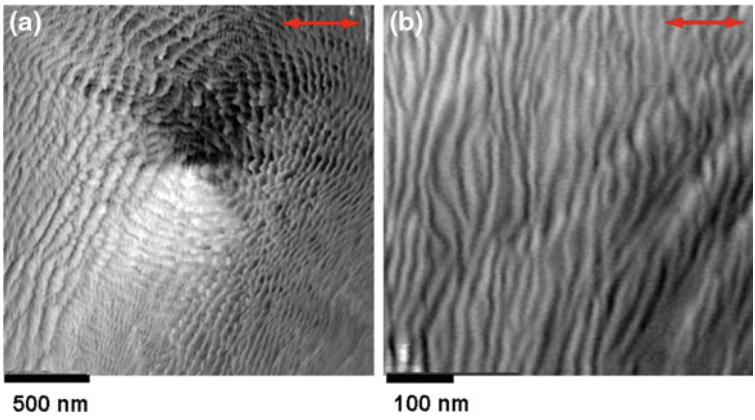

Fig. 1.3 SEM micrographs of the *central* part of an ablation crater on CaF_2 (10,000 pulses@8.4 TW/cm^2) exhibiting: **a** radial spreading coarse overstructure and **b** fine ripples

1.1.2 Modeling of Ripples Formation

Experimental observation of ripples over such wide range of materials and over a large wavelength interval has been accompanied by intensive theoretical studies; however, the underlying physical mechanisms are not yet fully understood. Presently, two basically different approaches are discussed in the literature.

The "classical" approach assumes that a lithography-like *modulated energy deposition*, caused by some optical interference, is imprinted into a corresponding ablation pattern and thus results in a modulated surface morphology, as shown in Fig. 1.4a [29–31]. In that model, ripples appear in the areas, where the absorbed energy is largest, and the formation process is lithography-like, where the irradiated material only plays a *passive* role. Another approach, schematically presented in Fig. 1.4b, known as a *self-organization model* [24, 32], is based on the dynamics of ultrashort pulse laser interaction with the target material [33, 34], and is inspired by the similarity of the laser generated patterns with those observed in very many other fields in nature, in particular in surface sputtering by energetic ions [35]. The model supposes an *active* contribution of the irradiated material: The absorbed laser energy causes a perturbation and softening of the crystal binding, leading to an unstable surface region, which relaxes via self-organization and, as a consequence of this, a spontaneous formation of surface structures in the laser-modified area [36, 37].

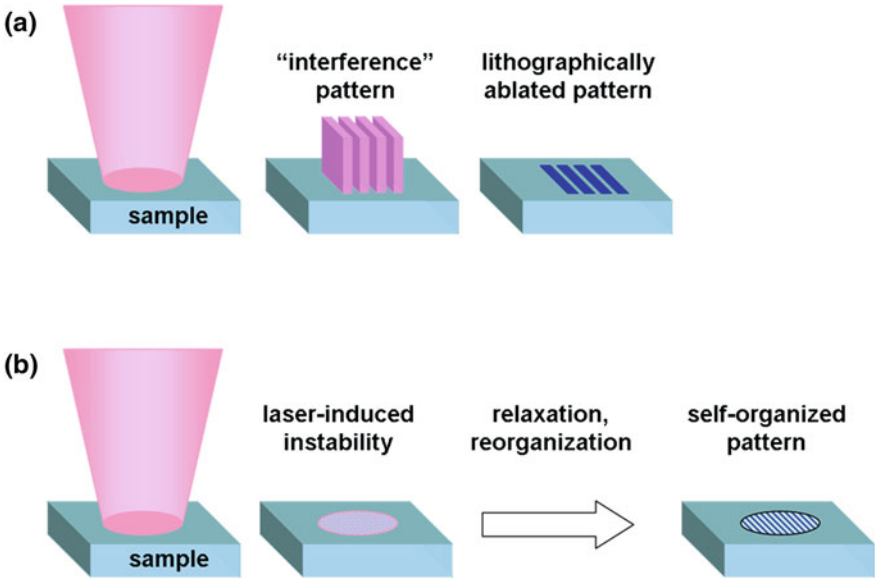

Fig. 1.4 Different approaches of LIPSS formation: **a** spatially modulated energy deposition ("interference" pattern) results in modulated ablation; **b** "self-organization model": femtosecond laser beam induces a high degree of instability at the surface; the perturbated surface relaxes through reorganization that leads to formation of self-organized pattern in the laser-affected region

1.1.2.1 Weakness of the Classical Theory

The theoretical approach based on a modulated energy deposition was in good agreement with many experimental data published at that time [4, 31]: the "interference" model described very well structures consisting of long, almost parallel lines, resembling very much a typical interference pattern, with periods close to the laser wavelength. These LIPSS are often called "LSFL" ("low spatial frequency LIPSS") [20], to be distinguished from the femtosecond laser-induced ripples, termed as "HSFL" ("high spatial frequency LIPSS"), with periods much smaller than the laser wavelength. Such fine ripples constitute the major deficiency of the "classical" approach, because they cannot be explained by an optical interference effect. To overcome this problem, additional interactions have been introduced in the model. At first, optical properties of the excited target material were taken into account by an adaptable (by an adjustable density of surface free electrons) refractive index of the surface selvedge [12, 38]. Further, the "surface scattered field" in the classical approach was modified to include short-wavelength irradiation, e.g. by the generation of higher harmonics [20, 39, 40] or excitation of high-frequency surface plasmon polaritons [18, 19, 41]. As a consequence, the actual version of the model proposes *different* interaction mechanisms for different kinds of structures.

Though some progress has been made, and the models mentioned above could approximately account for the ripple periods of subwavelength range, they are not appropriate to explain other complex features, as, e.g., the dependence of the ripple period on the absorbed laser fluence, as well as multiple bifurcations, coarsening, including period doubling, showing up in femtosecond laser ablation experiments. Despite all updating, the classical approach is, nevertheless, unable to explain a diversity of complex patterns, such as cones, "bubbles", or larger formations (macro structures), observed by femtosecond laser ablation. In particular, patterns induced by circularly polarized irradiation cannot at all be interpreted in framework of this model.

1.1.3 Self-organization as Origin of LIPSS

Analysis of the experimental observations, especially the variety of typical structures shapes and sizes, as well as their complex morphology indicates that femtosecond LIPSS are very similar to other self-organized patterns originating from instabilities such as, e.g., ripples produced by ion beam sputtering (IBS) [42].

A detailed comparison of surface morphologies generated by IBS and fs laser ablation (see Fig. 1.5) reveals very strong similarity in the shapes (bifurcating long linear structures) and ripples wavelength ($\Lambda \sim 200 \div 300$ nm). Additionally to the visual affinity of the patterns, other common features are found such as, for instance, the dependence of the ripples period on the irradiation dose, namely, on ions' energy and irradiation time for IBS [43] and laser intensity and number of pulses in case of laser ablation [10, 44]; or the important role of positive feedback in

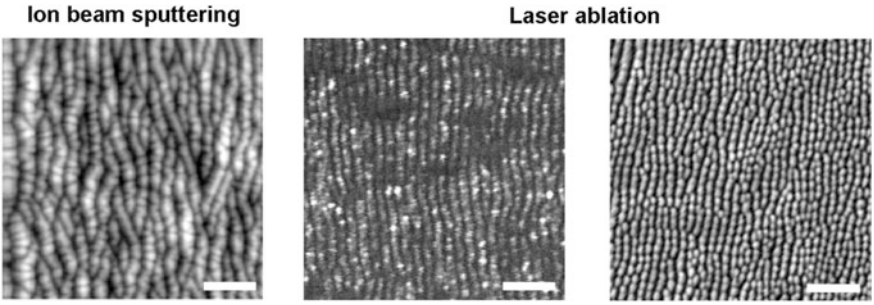

Fig. 1.5 Ripples induced upon *Ion beam sputtering* and femtosecond *Laser ablation*. The *left image*: AFM micrograph of ripple pattern generated on silicon with Ar+ ion beam [42]; in the *middle*: SEM image of ripples structures at the *bottom* of an ablation crater produced on silicon with 60,000 pulses at 0.4 TW/cm^2 [13]; the *right image*: SEM micrograph of the ripples induced on CaF_2 surface upon 5,000 pulses, 8 TW/cm^2. The *bar scale* at the micrographs indicates 1 μm

the development and formation of the pattern [23, 42]; or the coexistence of coarse and fine ripples with stepped changing of the periodicity ("period doubling") [26]. All this suggests to assume a similar mechanism of ripples formation by energetic ion beam and ultrashort pulsed laser irradiation.

1.1.3.1 Patterns Originating from Instability

Pattern formation from instability is very well known as a general natural phenomenon, and it has been intensively studied in various areas of basic and applied science. In nature, ripples can be observed in sandy deserts [45] and on the sea-bottom [46] as a result of interaction between sand grains and wind or shallow wavy water, and even on Mars [47]. In physics, the pattering behavior can be found in different areas of material processing, such as ion-beam sputtering [42], thin film deposition [48], or as in our case, as a result of femtosecond pulse laser ablation.

After a physical system has been driven into instability, i.e. a state which is not in thermodynamic equilibrium, the system has to move toward a new stable state by some intrinsic nonlinear mechanisms involving positive feedback. The physics of pattern formation can be described within the theoretical framework of nonlinear dynamics. Spatial and temporal evolution of a perturbed system is generally represented by nonlinear partial differential equations, for example equations of the Kuramoto-Sivashinsky/Kardar-Parisi-Zhang type [49–51]. The solution of such equations with corresponding boundary conditions results in the pattern formation. Understanding of the physical background in the patterning behavior must include the study of mechanisms how some small effects can govern the dynamics of pattern formation. That is the great scientific challenge.

Attributing the "femtosecond" ripples to the universal phenomenon of spontaneous pattern formation arising from instabilities, we want first to review the well known description of surface pattering by IBS.

1.1.3.2 Pattern Formation Upon Ion-Beam Sputtering (Review)

When a high-energetic ion beam impacts on a target surface, it will penetrate into the solid and transfer its kinetic energy and momentum to the lattice atoms through cascades of collisions [52]. The volume excited by these ballistic processes is approximately an ellipsoid with the major axis along the incident ion beam direction (Fig. 1.6). During this process, lattice atoms can be displaced from their equilibrium position or, if the transferred energy is sufficient to overcome binding energy, ejected or sputtered from the target.

The volume perturbed by the collisions depends on the energy and mass of the bombarding ions and on the mass of the target atoms. The amount of sputtered atoms, or sputtering yield, is a function of the incident ion flux and of the local surface curvature. Erosion of a corrugated surface by an ion beam is shown in Fig. 1.6a. Let us consider the dissipation of energy, deposited at point P, to the target surface. The average energy transferred to O' is greater than at O, $\mathrm{E}(O') > \mathrm{E}(O)$, that means that the erosion velocity of the valleys is larger than at the crests, $\upsilon(O') > \upsilon(O)$ [55]. Thus, the inhomogeneous erosion increases the amplitude of the corrugation and leads to an instability. To complete the surface evolution, thermal atomic self-diffusion activated by the irradiation should be taken into account. These competing processes, surface erosion and diffusion of target atoms, result in ripple pattern formation.

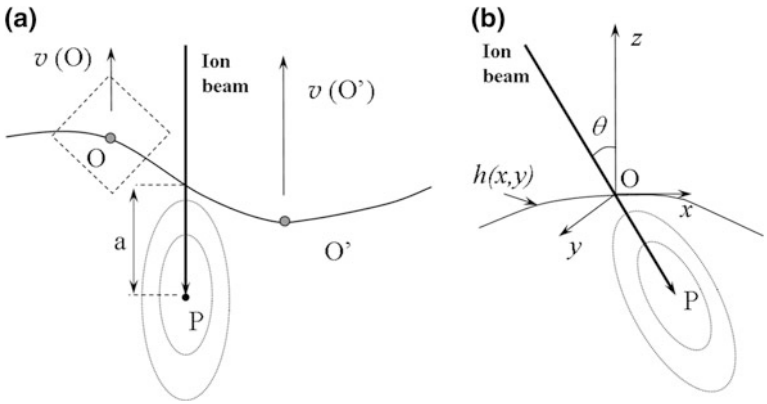

Fig. 1.6 Erosion of a corrugated surface by an ion beam. **a** The incident ion beam (*bold solid arrow*) penetrates an average distance a inside the solid and will be stopped at point P due to collisions, losing kinetic energy. O and O' are surface atoms on the crest and in the valley, correspondingly. P is the point of energy deposition; the *dotted ellipses* show contours of equal energy deposition (after [53]). **b** Ion erosion at point O (indicated with a *dashed square* in (**a**)) is shown in *local* coordinates (after [54])

The first theoretical approach, describing ripple formation by ion-beam sputtering, has been proposed by Bradley and Harper [55]. The modeling exploits the dependence of the erosion velocity [52], υ, on the average energy deposited at a point P(x, y, z) by an ion (Fig. 1.6b). Taking into account that the erosion velocity, υ, is a function of incidence angle, θ, and a local surface curvature, R, and adding a surface self-diffusion term, we obtain the time evolution of the growing surface profile $h(x, y)$:

$$\frac{\partial h}{\partial t} = -\upsilon(\theta, R)\sqrt{1 + (\nabla h)^2} - K\nabla^2\left(\nabla^2 h\right) \tag{1.1}$$

Now, let us consider the first term on the right-hand side of (1.1). As indicated in Fig. 1.7, removal takes place in a direction locally normal to the interface. When a particle is removed, the increment, $\upsilon\Delta t$, projected along the h axis is Δh. Following the geometry of the problem, from a right triangle we find Δh as (cf. Fig. 1.7):

$$\Delta h = \left[(\upsilon\,\Delta t)^2 + (\upsilon\,\Delta t\,\tan\alpha)^2\right]^{1/2} \tag{1.2}$$

Taking into account that $\tan\alpha = \frac{dh}{dx}$, (1.2) results in the first term of (1.1):

$$\frac{\partial h}{\partial t} = \upsilon\left[1 + (\nabla h)^2\right]^{1/2} \tag{1.3}$$

The second term on the right-hand side in (1.1) describes the surface self-diffusion of atoms, where the diffusion coefficient K is given by

$$K = \frac{D_S \gamma v}{n^2 k_B T}\exp\left(-\frac{\Delta\varepsilon}{k_B T}\right) \tag{1.4}$$

Here D_S is the surface self-diffusivity, γ the surface free energy per unit area, v the real density of diffusing atoms and $\Delta\varepsilon$ the activation energy for surface self-diffusion [55].

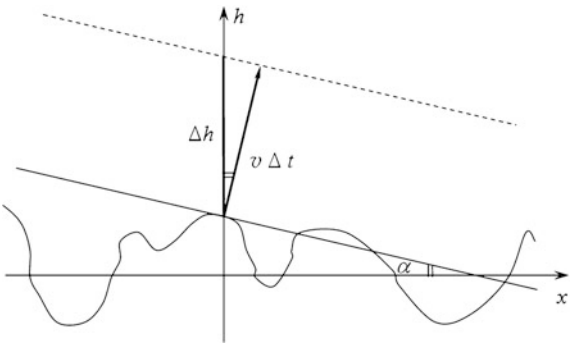

Fig. 1.7 Influence of a surface local curvature on the erosion velocity $\upsilon(h)$ (analogous to [51])

Equation (1.1) is an equation of Kardar-Parisi-Zhang type, and its solution predicts the formation of periodic surface structures with orientation and wavelength Λ depending on the incident angle of the ion beam, θ, and, in special cases, depending on the surface temperature, T, diffusion coefficient, K, and the activation energy for surface self-diffusion, $\Delta\varepsilon$:

$$\Lambda(\theta) \propto \frac{K}{\sqrt{T}} \exp\left(-\frac{\Delta\varepsilon}{k_B T}\right) \tag{1.5}$$

1.1.3.3 Ultrashort Pulsed Laser Induced Surface Instability

The physical processes of femtosecond laser ablation indicate the generation of a considerable instability at the irradiated surface. The rapid excitation of electrons by the incident laser electric field induces a softening of the atomic bonds [56] through redistribution of the deposited energy on a time scale about of several 100 fs leading to a destabilization of the crystal lattice [57]. Additionally, the surface equilibrium order can be disturbed due to emission of individual components (ions, atoms, clusters). As a result, the target lattice is strongly perturbed on a very short time scale,[1] i.e. the system is strongly unstable and very far from thermodynamic equilibrium. This nonequilibrium in the system must rapidly relax via a macroscopic material removal and surface restructions. The rapid relaxation is provoked by a steep gradient in crystalline order to the surrounding material and is too fast for any thermal processes [58].

Like a pattern induced by surface bombardment with an energetic ion beam, we attribute such structure formation to a surface self-organization from a high degree of instability induced by irradiation with an ultrashort laser beam. But, in contrast to ion sputtering, when the erosion of the surface takes place *during* ion bombardment and proceeds continuously, femtosecond laser ablation is a pulsed process. Energy input and desorption/rearrangement of massive particles are temporally well separated. Consequently, the impact of intense ultrashort pulse on solid surface results in a few different regimes shown in Fig. 1.8.

This scheme shows the time scales of secondary processes activated in a transparent dielectric crystal by irradiation with a 120-fs laser pulse of 800 nm at intensity well below the single-shot ablation threshold [59]. The incident light first only excites the electrons of the system, their appreciable emission is observed during the pulse. In a second, presumably delayed step, the actual ejection of fast ions (Coulomb/phase explosion) occurs, after a transfer of electronic excitation to the lattice. With the emission of slow/thermal ions begins the last step, namely, the thermal relaxation on a larger timescale through thermal conductivity effects/thermal self-diffusion of atoms.

[1] Similar to a melt, but not relaxed to thermodynamic equilibrium.

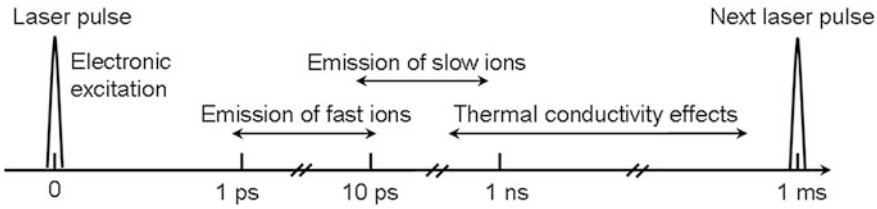

Fig. 1.8 Typical time scales of various secondary processes stimulated by irradiation of transparent dielectrics by a femtosecond laser pulse

1.1.3.4 Time Evolution of Surface Profile Upon Repetitive Irradiation

In this section we consider the creation of a thin corrugated layer on the surface of irradiated target upon multiple ultrashort laser pulses. For simplicity, let's restrict to a dielectric crystal. Initially, the surface of the target is assumed to be ideally plain.

When the laser beam hits a plain surface, a stochastic charge distribution and, hence, an ion emission from randomly located sites, resulting in the creation of the local defects, can occur in the irradiated area. A higher absorption probability in the defect states will result in a progressively inhomogeneous surface ionization upon the following laser pulses. The conception of the corrugated surface layer is shown schematically in Fig. 1.9: small symmetry breaking irregularities on the initially plain surface develop to the modulated surface layer upon multipulse irradiation. The process is highly nonlinear and boosted by a positive feedback.

After several more laser pulses, a modulated, thin surface film of thickness a and modulation height $h(x, y)$ builds up (Fig. 1.10). The absorption cross-section of the film is tending towards a more homogeneous with each subsequent pulse. Desorption, however, is not homogeneous and depends on a local surface-curvature. Assuming Coulomb explosion, e.g., as the possible ablation mechanism, we can see that for a uniform surface charge density, the ion sitting in a valley (Fig. 1.10) has the higher density of (charged) neighbors than an ion on a crest. The higher next-neighbor density results in the stronger repulsion (Coulomb) force and, consequently, in a larger escape velocity of valley-ions, υ_{valley}, compared to that

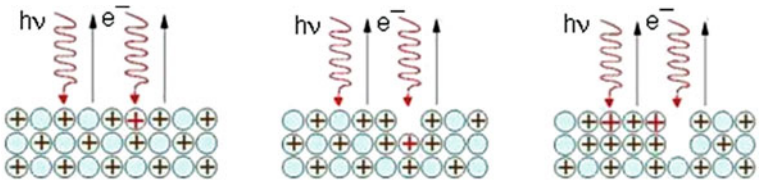

Fig. 1.9 Development of a corrugated surface layer upon multipulse laser irradiation. Incident laser light ($h\nu$) is shown with *waved arrows*; emission of photoelectrons (e^-) is indicated with *vertical arrows*

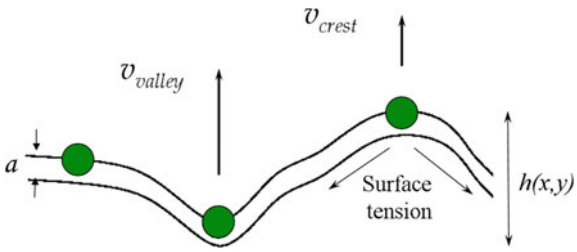

Fig. 1.10 Model for surface height evolution: a is the thickness and $h(x, y)$ is the modulation height of an unstable surface film induced upon repetitive laser irradiation. Velocities of the desorbed ions from the valley (v_{valley}) and from the crest (v_{valley}) are indicated with *arrows*

from crests, v_{crest}. So, valleys will be faster eroded than crests, this causes instability of the thin surface film, very similar to the case of ion sputtering (Fig. 1.6).

Balancing the surface erosion process, thermally activated self-diffusion tends to smooth the surface again by filling the valleys with diffused crest-atoms. Moreover, in the thin unstable layer the particle on the crest will feel a higher surface tension than in the valley. The tension gradient forces the particles to downhill moving and balances thereby the instability on the surface.

Thus, the time evolution of the growing surface profile can be described by the elementary processes taking place in the system: surface erosion (roughening) due to particle emission and smoothing due to atomic self-diffusion.

1.2 Laser Polarization in the Model of Self-organization

Numerous experimental results have revealed a strong dependence of ripples orientation on the polarization of the incident laser field. By taking into account that an ultrashort laser pulse is addressed just to the electronic system of solids and the subsequent energy transfer to the lattice occurs on the timescale of electron-phonon relaxation [60] that is significantly larger than the laser pulse duration, the understanding of the puzzling relation between pattern orientation and laser polarization, i.e. the direction of the electromagnetic field vector, becomes very important and interesting.

In the following, this dependence is analyzed within an adopted surface erosion model, based on the description of ion beam sputtering [55]. A continuum theory of erosion by polarized laser irradiation is developed. In particular, the dependence of generated patterns on the laser polarization is considered.

1.2.1 Model

The geometry of the model is illustrated in Fig. 1.11. In the figure are shown the laboratory frame (x, y, h) with h perpendicular to the *flat* substrate, the *local* surface frame (X, Y, Z) taking into account surface corrugation with radius R, and the frame (x', y', z') connected with the incident laser beam propagating in the direction parallel to z', as well as azimuthal and elevation angles connecting these frames. The laser beam is incident on the target surface and is absorbed in some point P, from where its energy is further transferred (cf. dotted ellipses in Figs. 1.11 and 1.13) to the neighboring sites. Though the incidence angle of the beam can vary (cf. Fig. 1.6b), here, for simplicity, we consider normal incidence to the flat surface.

Following Peter Sigmund's theory of ion sputtering [52], we can relate the erosion velocity normal to the surface to the energy input:

$$\upsilon \cong \xi \int_V dr^3 \psi(r) \varepsilon(r) \tag{1.6}$$

where the integration is performed over the volume V, including all points, at which the deposited energy contributes to the erosion velocity υ at the surface. ξ is a material parameter, $\psi(r)$ takes into account local variations of the deposited energy due to attenuation, refraction and reflection. In principle, $\psi(r)$ contains all information about spatial beam profile, absorption cross section, and losses along the beam pass to reach $P(r)$. ε (r) is the fraction of that energy, dissipated to the surface

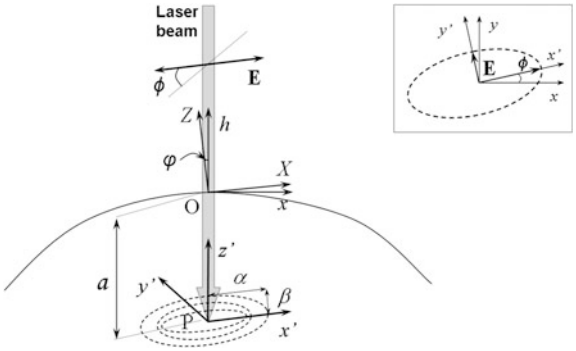

Fig. 1.11 Reference frames for the computation of the erosion velocity: (x', y', z') is the reference frame of the incoming beam, x' is parallel to the vector **E** of the electromagnetic field; (X, Y, Z) corresponds to the local coordinate frame, where Z is parallel to the local normal to the surface, while (x, y, h) denotes the laboratory frame of coordinates with h perpendicular to the flat substrate surface. The *dotted ellipse* is a Gaussian distribution of deposited energy with half-width α, β along x', y', respectively. The energy distribution along z' with half-width γ is not shown here. φ is the angle between the local and the laboratory reference frames (corrugation) and denotes the "local" incidence angle; ϕ is orientation of **E** in the plane of incidence (x, y). *Inset* View from *top* along h

after absorption at $P(r)$ and resulting in erosion. To evaluate $\varepsilon(r)$, we have to take into account the dynamics of femtosecond laser-matter interaction.

Similarity of the laser-induced instability on the target surface to the well-known hydrodynamic instability of thin liquid films (cf. Sect. 1.1.3.1) allows us to use an analogous approach as in that case and to describe the time evolution of the surface height profile $h(x, y, t)$, caused by surface erosion [35], with the (1.1), where the erosion velocity is a function not only of the local surface curvature (φ, R) and of the incident angle of the laser beam (θ) (cf. Fig. 1.7), but depends also on the orientation of the laser electric field denoted with angle ϕ in Fig. 1.11.

1.2.1.1 The Role of Anisotropic Excitation

The absorbed laser energy results only in an excitation of electrons. In dielectrics and semiconductors, electrons are excited from the valence to the conduction band. These electrons thermalize their kinetic energy first by collisions with the other conduction electrons and then, only subsequently, transfer the energy to the lattice by electron-phonon collisions.

One possible origin of an asymmetry in such energy transfer is based on the initial photoionization, i.e. the excitation from the valence into the conduction band. It is well known from the photoionization of free atoms that the electric light field results in an asymmetric distribution of electron kinetic energy: their velocity is larger in the field direction and less in all other directions. On the other hand, the electron mean free path strongly depends on their kinetic energy [61] and decreases more than one order of magnitude in the range between 0.5 and 10 eV [58], as a consequence of a reciprocal variation of collision-and thus energy transfer-probability (Fig. 1.12).

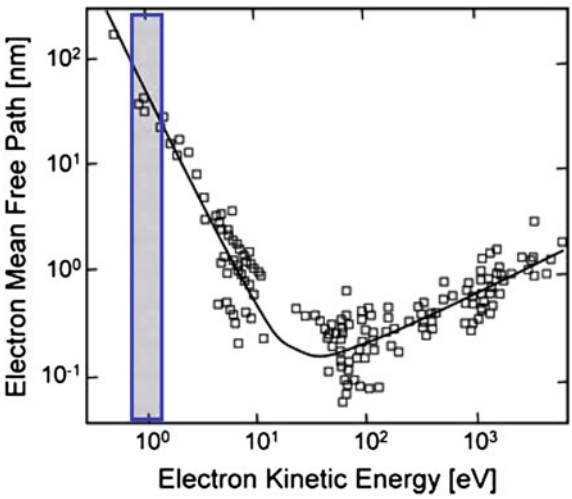

Fig. 1.12 The "Universal Curve" of electron mean free path versus electron kinetic energy. The *grey area* indicates the region of typical kinetic energies in the considered situation (from [58])

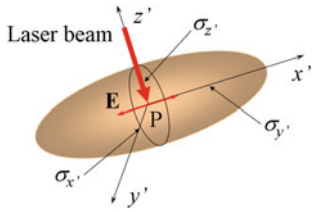

Fig. 1.13 The *ellipse* illustrates the cross sections of relative collisional energy transfer after laser excitation at point P in the frame of incoming beam (x', y', z'). *Linear* polarized *laser beam* propagates along z'; vector **E** defines the direction of linear polarization (**E**$\|x'$)

Consequently, assuming Gaussian velocity distributions for the electrons, we can approximate the contribution of energy absorbed at P to the erosion velocity:

$$\varepsilon(r') = \chi \exp\left\{-\frac{1}{l^2}\left[\left(\frac{x'^2}{\sigma_{x'}}\right) + \left(\frac{y'^2}{\sigma_{y'}}\right) + \left(\frac{z'^2}{\sigma_{z'}}\right)\right]\right\} \tag{1.7}$$

Here l is the electron mean free path at low electron energy (close to the bottom of the conduction band) and it is proportional to a in Fig. 1.11; χ is a material parameter; and σ_k are the relative energy coupling cross sections in k direction ($k = x'$, y', z') (Fig. 1.13) and thus reciprocal to the relative mean free path, α, β and γ in Fig. 1.11.

Another possible reason for the anisotropic energy transfer is the resonant excitation of surface plasmon-polaritons (SPPs) on a corrugated interface conductor/vacuum [18, 41], where absorption is largest for **E** parallel to the k-vector of the corrugation.

1.2.1.2 Equation Describing an Evolution of the Surface Profile

Let's return to the problem of the time evolution of the surface height profile as described in Fig. 1.11. Whereas in Sigmund's theory [52] the parameters α, β and γ along x', y' and z', respectively, are scaled as $\alpha = \beta \geq \gamma$, in the case of light-matter interaction we do not have anymore the same constant ratio between these three components. The relation between α and β depends on the characteristics of irradiation, absorption and dissipation; and γ is a constant that corresponds to a thin layer a (cf. Figs. 1.10 and 1.11), generally determined by the mean free path of conduction band electrons.

Following to [35, 55] we have to perform the calculation of the erosion rate in the local coordinate system (X, Y, Z). This means that we need to transform the deposited energy $\varepsilon(r)$ (1.7) from (x', y', z') to the local (X, Y, Z) reference frame by a rotation:

$$\begin{pmatrix} x' \\ y' \\ z' \end{pmatrix} = \begin{pmatrix} \cos\phi\cos\varphi & \sin\phi & \cos\phi\sin\varphi \\ -\sin\phi\cos\varphi & \cos\phi & -\sin\phi\sin\varphi \\ -\sin\varphi & 0 & \cos\varphi \end{pmatrix} \cdot \begin{pmatrix} X \\ Y \\ Z \end{pmatrix} \tag{1.8}$$

and subsequent translation along the beam direction by the value a. To simplify our consideration we restrict our calculations to the case of small incident angles θ in optically transparent materials. The local correction to the incident energy flux is now given by $\psi(r) = \mathrm{A} \cdot I_0\left(\cos\varphi + \left(\partial Z/\partial X\right)\sin\varphi\right)$, where A is the generalized absorption coefficient[2] of the material and I_0 is the laser intensity. In order to describe the surface profile in the neighborhood of O (Fig. 1.11), we take into account cross-terms of the type $\sim XY$

$$Z(X,Y) \cong -\frac{1}{2}\left(\frac{X^2}{R_X} + \frac{Y^2}{R_Y}\right) - \frac{XY}{R_{XY}} \tag{1.9}$$

As in [35] we assume that the radii of curvature R_X, R_Y and R_Z of the surface are much larger than a, which in this case means the distance from the surface to the absorption point P, so that only terms up to first order in a/R_X, a/R_Y and a/R_Z are kept. The integration results in the erosion velocity $\upsilon(\varphi, \phi, R_X, R_Y, R_{XY})$ as a function of angles φ, ϕ, and the curvatures:

$$\frac{1}{R_X} = -\frac{\partial^2 Z}{\partial X^2}, \qquad \frac{1}{R_Y} = -\frac{\partial^2 Z}{\partial Y^2}, \qquad \frac{1}{R_{XY}} = -\frac{\partial^2 Z}{\partial X \partial Y}. \tag{1.10}$$

Now, we examine the evolution of the surface corrugation $z = h(x, y, t)$ with time t, starting from an originally flat configuration ($h = 0$). We rewrite υ in terms of the laboratory coordinates (x, y, h) [35]:

$$\frac{\partial h(x,y,t)}{\partial t} = -\upsilon(\varphi, \phi, R_X, R_Y, R_{XY})\sqrt{1 + (\nabla h)^2} \tag{1.11}$$

We expand (1.11) in a Taylor series and complete it by adding surface self-diffusion (cf (1.1)) and the statistical fluctuations of initial surface roughness $\eta(x, y, z)$ (short noise). Finally, we obtain the equation of motion known as an anisotropic noisy Kuramoto-Sivashinsky [49, 50] equation:

$$\begin{aligned} \frac{\partial h}{\partial t} = &-\upsilon_0 + \nu_x \frac{\partial^2 h}{\partial x^2} + \nu_y \frac{\partial^2 h}{\partial y^2} + \nu_{xy} \frac{\partial^2 h}{\partial x \partial y} \\ &+ \frac{\lambda_x}{2}\left(\frac{\partial h}{\partial x}\right)^2 + \frac{\lambda_y}{2}\left(\frac{\partial h}{\partial y}\right)^2 + \frac{\lambda_{xy}}{2}\left(\frac{\partial h}{\partial x}\right)\left(\frac{\partial h}{\partial y}\right) \\ &- K\nabla^2\left(\nabla^2 h\right) + \eta(x,y,z), \end{aligned} \tag{1.12}$$

[2] Note that, for multiphoton absorption in transparent media, A will be of the form $\mathrm{A}_0\mathrm{I}^{n-1}$.

where the coefficients are now the complex functions of the two angles ϕ and θ. For the case of normal incidence illustrated in Fig. 1.11, the coefficients take the form:

$$\begin{aligned}
v_x &= -\frac{Fa}{2\gamma}\left(\frac{\alpha^2}{\gamma^2}\cos^2\phi + \frac{\beta^2}{\gamma^2}\sin^2\phi\right),\\
v_y &= -\frac{Fa}{2\gamma}\left(\frac{\alpha^2}{\gamma^2}\sin^2\phi + \frac{\beta^2}{\gamma^2}\cos^2\phi\right),\\
v_{xy} &= -\frac{Fa}{2\gamma}\left(\frac{\beta^2}{\gamma^2} + \frac{\alpha^2}{\gamma^2}\right)\sin 2\phi,\\
\lambda_x &= -\frac{F}{\gamma}\left[1 + \left(\frac{\alpha^2}{\gamma^2} - 1\right)\left(\frac{\alpha^2}{\gamma^2}\cos^2\phi + \frac{\beta^2}{\gamma^2}\sin^2\phi\right)\right],\\
\lambda_y &= -\frac{F}{\gamma}\left[1 + \left(\frac{\alpha^2}{\gamma^2} - 1\right)\left(\frac{\alpha^2}{\gamma^2}\sin^2\phi + \frac{\beta^2}{\gamma^2}\cos^2\phi\right)\right],\\
\lambda_{xy} &= -\frac{F}{\gamma}\left(\frac{\alpha^2}{\gamma^2} - 1\right)\left(\frac{\beta^2}{\gamma^2} - \frac{\alpha^2}{\gamma^2}\right)\sin 2\phi,\\
v_0 &= \frac{F}{\gamma}
\end{aligned} \tag{1.13}$$

and $F = \frac{I_0 \xi \mathrm{A}}{\sqrt{2\pi}} \exp\left(\frac{\alpha^2}{2\gamma^2}\right)$.

In order to extract the physical meaning from (1.12) and (1.13), we consider, in this approach, the special case $v_{xy} = 0$ and $\lambda_{xy} = 0$. That means (1.12) and (1.13) are taken in the reference frame rotated by the angle ϕ (cf. inset in Fig. 1.11). Moreover, we neglect here the erosion velocity of the initial flat surface vi_0, which does not effect the size of ripples and can be eliminated by the transformation $\tilde{h} = h + vi_0 t$.

$$\frac{\partial h}{\partial t} = v_x\frac{\partial^2 h}{\partial x^2} + v_y\frac{\partial^2 h}{\partial y^2} + \frac{\lambda_x}{2}\left(\frac{\partial h}{\partial x}\right)^2 + \frac{\lambda_y}{2}\left(\frac{\partial h}{\partial y}\right)^2 - K\nabla^2\left(\nabla^2 h\right) + \eta(x,y,z), \tag{1.14}$$

where the coefficients are given now by

$$\begin{aligned}
v_{x,y} &= -\frac{F}{2}\sigma_\gamma \Omega_{x,y}\\
\lambda_{x,y} &= -\frac{F}{\gamma}\left[1 + \left(\sigma_\gamma^2 - 1\right)\Omega_{x,y}\right]
\end{aligned} \tag{1.15}$$

and

$$\begin{aligned}
&\Omega_{x,y} = \Delta[1 \pm \Pi]; \qquad \Delta = \frac{1}{2}\left(\frac{\sigma_\gamma^2}{\sigma_\alpha^2} + \frac{\sigma_\gamma^2}{\sigma_\beta^2}\right); \qquad \Pi = \frac{\sigma_\beta^2 - \sigma_\alpha^2}{\sigma_\beta^2 + \sigma_\alpha^2};\\
&\sigma_i = \frac{a}{i}(i = \alpha, \beta, \gamma)
\end{aligned} \tag{1.16}$$

Polarization parameter Π describes an asymmetry of energy distribution in ($x'y'$) plane, *depth parameter* Δ takes into account energy deposition also along z' axis (Fig. 1.11), connected with the direction of laser beam propagation. Combinations of Π and Δ result in *anisotropy parameter* Ω in (1.16) that determines the spatial asymmetry in energy distribution at point *P*.

1.2.2 Linear Stability Analysis

In this section the basic role of polarization and depth parameters, Π and Δ, will be explained by means of a linear stability analysis of (1.14). For this purpose, we introduce a periodic perturbation $h = h_0 \exp\{i(q_x x + q_y y - \omega t) + \sigma t\}$ and obtain the normalized growth rate

$$\frac{1}{h_0}\frac{\partial h}{\partial t} = \Sigma = -\left[v_x q_x^2 + v_y q_y^2 + K\left(q_x^2 + q_y^2\right)^2\right]. \tag{1.17}$$

From (1.15) and (1.16) follows that polarization and depth parameters contribute to the two tension coefficients $v_{x,y}$, which are negative for normal incidence and in general are not equal to each other due to the fact that Π increases v_x and reduces v_y. Figure 1.14 shows the linear growth rate Σ along perturbation wave vectors q_x and q_y for various values of parameters Δ and Π. For Δ = 0 the uniform state is stable ($v_x = v_y = 0$), whereas for nonzero Δ and Π = 0 we obtain equal instability along q_x and q_y ($v_x = v_y = -(F\sigma_\gamma/2)\Delta$). Distinct from zero, the value of Π induces an asymmetrical instability in the q_{xy}-plane with the wave vector:

$$q_{x,y}^* = \sqrt{\frac{F\sigma_\gamma}{4K}\Delta[1 \pm \Pi] - q_{y,x}^2} \tag{1.18}$$

An increase of Π shifts the instability to higher values of q_x ($v_x = -(F\sigma_\gamma/2)\Delta[1 + \Pi]$) and suppresses the instability along q_y ($v_x = -(F\sigma_\gamma/2)\Delta[1 - \Pi]$). Thus, for $\Pi \sim 1$ the instability along q_y disappears.

From the stability analysis of Fourier modes for (1.14) we expect the instability for the ripple formation with wavelength $\Lambda_i = 2\pi\sqrt{2K/|v_i|}$, where i refers to the x or y direction along which the corresponding v_i is largest. Thus, in the case of $v_x < v_y < 0$, which holds when $0 < \Pi < 1$, the ripple structure is oriented in x direction with the following wavelength of the surface modulations:

$$\Lambda_{x,y} = 4\pi\sqrt{\frac{K}{F\sigma_\gamma\Delta(1 \pm \Pi)}} \tag{1.19}$$

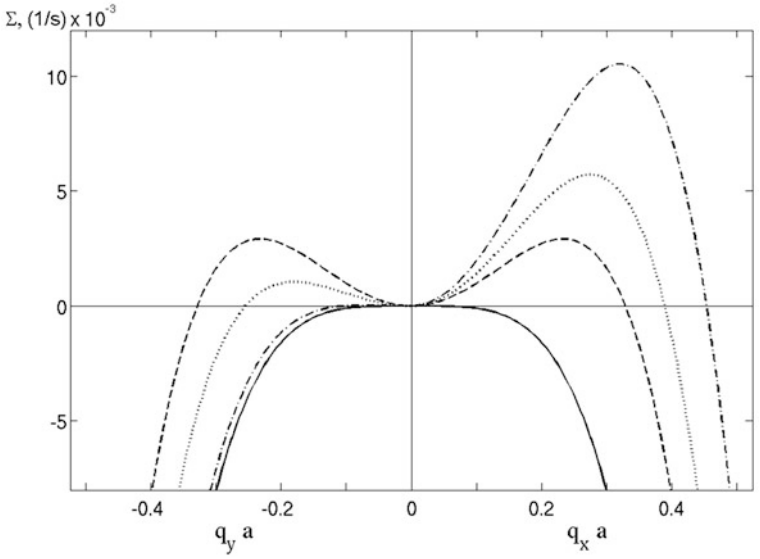

Fig. 1.14 Growth rate Σ as a function of a two dimensionless wave vectors $q_x a$ and $q_y a$ for various values of parameters Δ and Π: Δ = 0, Π = 0 (*solid line*); Δ = 1, Π = 0 (*dashed line*); Δ = 1, Π = 0.4 (*dotted line*); Δ = 1, Π = 0.9 (*dash-dotted line*)

For "zero" polarization parameter (Π = 0) the wavelength of ripple along x and y axis are equal: $\Lambda_x = \Lambda_y$. An increase of Π slightly reduces Λ_x whereas Λ_y becomes to be very large for $\Pi \rightarrow 1$. Equation (1.19) has revealed an influence of polarization parameter Π on the experimentally measured ripples characteristics Λ_x, Λ_y (period and bifurcation length). From the relation $\Lambda_x/\Lambda_y = \sqrt{(1-\Pi)/(1+\Pi)}$ the polarization parameter Π and, correspondingly, polarization of the incident laser field, can be determined.

We can consider the polarization parameter as a control parameter that represents a degree of anisotropy in the energy deposition and, therefore, the orientation of ripples formation. Indeed, from (1.16) Π = 0 corresponds to an equal energy deposition ($\alpha = \beta$, isotropic energy distribution) along x and y axes, whereas, $\Pi \sim 1$ describes the case $\alpha \gg \beta$ (energy flow in x, parallel to **E**).

To summarize, it has been shown that polarization parameter Π, characterizing the symmetry of the deposited energy distribution in the (x', y') plane (Fig. 1.11), determines orientation and also morphology of the calculated pattern. The anisotropy in the energy distribution is correlated with the vector **E** of incoming laser field in such a manner that **E** defines the preferred direction of the energy transfer. In the next subsection we discuss a morphological diagram and suppose to identify the direction of the preferred energy transfer with the vector of polarization **E**.

1.2.3 Morphological Diagram for the Ripple Orientation

Another quantity that can change the ripple orientation is the angle of incidence θ. It is very important to note, that the orientation of the ripple due to the polarization and due to the incidence angle θ can compete or work together. Such behavior is one prediction of this theory, which has been tested experimentally. The general expressions being too complicated, we present here v_x and v_y in the reference frame rotated by angle ϕ:

$$\begin{aligned} v_x &= -\frac{F\sigma_\gamma}{2\zeta^2}\left(\frac{\sigma_\gamma^2}{\sigma_\alpha^2}\right) \\ &\quad \times \left[\cos^2\theta - 2\sin^2\theta\left(1 - \frac{\sigma_\gamma^2}{2\zeta}\cos^2\theta\right)\left(\frac{\sigma_\gamma^2}{\sigma_\alpha^2}\right)\right], \\ v_y &= -\frac{F\sigma_\gamma}{2\zeta}\left(\frac{\sigma_\gamma^2}{\sigma_\beta^2}\right)\cos^2\theta, \end{aligned} \tag{1.20}$$

where $\zeta = \cos^2\theta + \left(\sigma_\gamma^2 \Big/ \sigma_\alpha^2\right)\sin^2\theta$ and by using (1.16) we express the $\sigma_\gamma^2 \Big/ \sigma_\alpha^2$ and $\sigma_\gamma^2 \Big/ \sigma_\beta^2$ in terms of Δ and Π:

$$\left(\frac{\sigma_\gamma^2}{\sigma_\alpha^2}\right) = \Delta(1+\Pi) \quad \text{and} \quad \left(\frac{\sigma_\gamma^2}{\sigma_\beta^2}\right) = \Delta(1-\Pi). \tag{1.21}$$

In contrast to ion beam sputtering [35, 55] the most important parameter that influences the orientation of ripples in our consideration is the polarization parameter Π. Therefore, we study here the (Π, θ) morphological diagram for different values of σ_y. The boundary in the diagram is defined by $v_x(\Pi, \theta) = v_y(\Pi, \theta)$ and separates the region I ($v_x < v_y$) with the ripples wave vector in y-direction and region II ($v_x > v_y$) with the ripples wave vector in x-direction.

We start to discuss the diagram from the bottom (the left Inset in Fig. 1.15), where for small θ the wave vector of ripples is aligned along **E** and is perpendicular to the component of the beam in the surface plane. Thus, for small θ the orientation of ripples is defined by **E** and the influence of the angle of incidence is not appreciable. With increasing of θ the growing angle of incidence supports the effect of polarization and the wave vector of ripples remains along **E** that is shown in the bottom of diagram in the right Inset.

In the case of weak polarization $-0.4 \leq \Pi < 0$ a reorientation of ripples in dependence on θ can be observed for $\sigma_y > 1$. Indeed, one can see from the diagram in the case of $\Pi = 0$ that the increase of θ from zero (normal incidence) to some finite values reveals two possibilities: the wave vector of ripples is aligned parallel

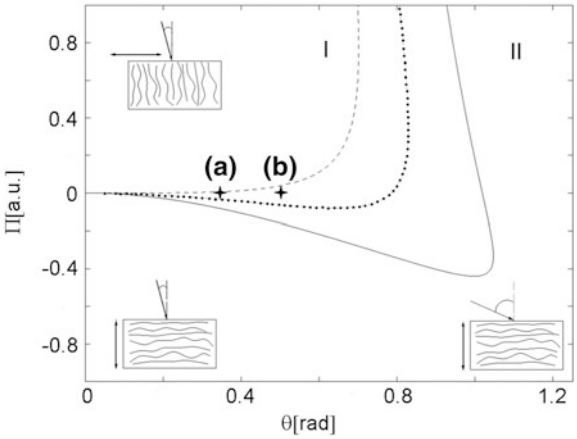

Fig. 1.15 Ripple orientation diagram presenting the boundary separating regions I ($v_x < v_y$) and II ($v_x > v_y$) for different values of $\sigma_y = 1$; 1.5; 2 (*dashed*, *dotted*, *solid line*, respectively). *Insets* show the incident angle, the direction of ripples and the vector **E** (*double arrows*). (*a*) and (*b*) correspond to the surface morphologies in Fig. 1.16

(perpendicular) to the component of incoming beam in the Region I (Region II) for $\sigma_y \leq 1$ ($\sigma_y > 1$). In the case of $\Pi = 0$ and at normal incidence some isotropic structures are expected in the model. This is also proved experimentally: at non-normal incidence an arrangement of nano-spheres typical for circular polarization (Fig. 1.1b) turns into a linear pattern with the wave vector of modulations oriented parallel to the incoming irradiation (Figs. 1.15 and 1.16). This comparison helps us to fix partially the parameter σ_γ for the following numerical calculations.

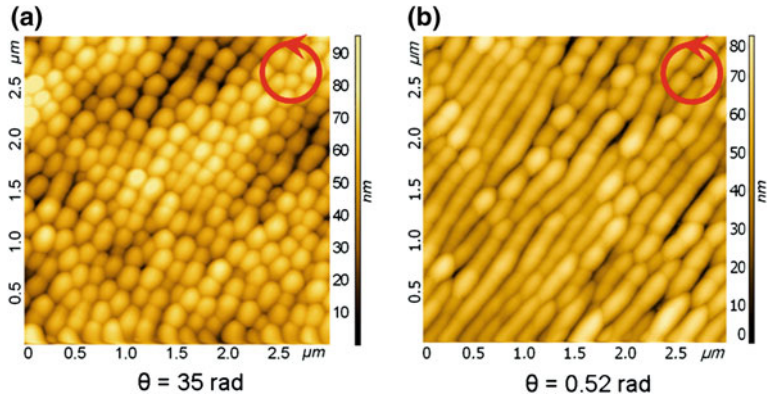

Fig. 1.16 Dependence of surface morphology on angle of incidence θ for *circularly* polarized beam: CaF_2 irradiated with 5,000 pulses at an intensity of about 8 TW/cm^2

1.2.4 Nonlinear Regime

Closer examination of (1.14) reveals that its time dependence consists of a linear part and nonlinear components. Let us consider the influence of the nonlinear terms λ_x and λ_y. As shown in [62], such separation of linear and nonlinear behavior in time assumes the existence of a crossover time t_c that separates these two regimes. In the linear regime up to t_c the nonlinear terms are negligible whereas they take over after

$$t_c \propto \left(\frac{K}{\nu^2}\right) \ln\left(\frac{\lambda}{\nu}\right) \tag{1.22}$$

and completely determine the surface morphology, which depends on the relative signs of λ_x and λ_y. The transition between linear and nonlinear regime is very abrupt and it is followed by the appearance of kinetic roughening. For $\sigma_y = 1.5$ both λ_x and λ_y are negative and depend on Π. The dependence of the crossover time on the polarization can be presented as follows:

$$t_c(\Pi) \propto \frac{t_c(\Pi = 0)}{(1 + \Pi)^2}, \tag{1.23}$$

where t_c is decreased with increasing of Π.

1.2.5 Influence of Polarization

Surface patterns obtained by numerical integration of (1.12) and corresponding Fourier images (2D-FTT) are presented in the upper row of Fig. 1.17. The morphologies are calculated for various ϕ, describing the orientation of the laser electric field $\mathbf{E}$ in the plane of incidence (x, y) (Fig. 1.11), and various values of polarization parameter Π, which can be associated with the polarization degree. The obtained numerical results show that an asymmetric energy deposition can describe the correlation of ripples orientation with laser polarization. The simulation time t is measured in arbitrary units (a.u.) and will be discussed in the next section. Note that, in contrast to the continuum evolution in the simulations, the experimental evolution is given by increasing the number of laser pulses.

In Fig. 1.17a we observe the surface morphology calculated for $\Pi = 1$, $(\sigma_\alpha \ll \sigma_\beta)$, $t = 800$ a.u. and $\phi = 0$. That means the energy distribution along x' is much larger than along y'. The pattern consists of periodic parallel lines, oriented perpendicular to $\mathbf{E}$. This is similar to the ripples produced by a linearly polarized laser beam (Fig. 1.17e). By rotation of vector $\mathbf{E}$ ($\phi = 45°$) for the same values of Π and t, the ripples follow the direction of incident electrical field (Fig. 1.17b) that is also in good agreement with experiment (Fig. 1.17f).

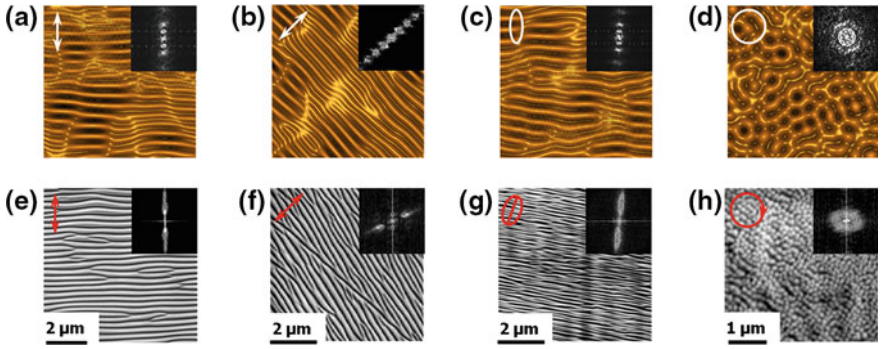

Fig. 1.17 The *upper panels* present numerically calculated surfaces of size $64\pi \times 64\pi$ in a.u., showing the surface morphologies for **a** $\phi = 90°$, $\Pi = 1$, t = 800 a.u.; **b** $\phi = 45°$, $\Pi = 1$, t = 800 a.u; **c** $\phi = 90°$, $\Pi = 0.5$, t = 1,400 a.u.; **d** $\phi = 90°$, $\Pi = 0$, t = 3,000 a.u.; *white double arrows* and *elliptical* figures define the energy distribution in the $(x'y')$-plane. The *bottom panels* exhibit ablation patterns on CaF_2 produced by 5,000 pulses at intensity 8 TW/cm^2 with *linear* (**e**, **f**), *elliptical* (**g**) and *circular* (**h**) polarization. The direction of incident electrical laser field is indicated with *double arrows*, *ellipse* and *circle*, respectively. The corresponding 2D-FFT images are presented in the *insets*

By variation of Π, between zero and one ($\sigma_\alpha < \sigma_\beta$), and fixed angle $\phi = 90°$ we create the configuration of elliptic polarization. The large axis of the polarization ellipse is oriented along y in the laboratory coordinate frame (x, y, h) (Inset in Fig. 1.11). As can be seen from Fig. 1.17c (t = 1,400 a.u.) the ripples are still aligned to the large axis of polarization ellipse, again good correlation with experiment for elliptic polarized irradiation (Fig. 1.17g). For $\Pi = 0$, ($\sigma_\alpha = \sigma_\beta$), i.e. circular polarization, we have a symmetrical energy distribution with respect to x' and y'. The calculated surface morphology for t = 3,000 a.u. does not posses linear order, the pattern is uniformly distributed (Fig. 1.17d). A similar kind of pattern, characterized by lack of linear order and consisting of arrays of uniformly distributed dots, is observed by laser ablation with circularly polarized pulses (Fig. 1.17h).

A detailed comparison and analysis of the 2D-FFT generated for the numerically simulated patterns (Fig. 1.17a–d) and for the SEM images of ablation morphologies (Fig. 1.17e–h) has revealed an excellent qualitative agreement between theory and experiment.

1.2.6 Period of Numerically Calculated Pattern

By irradiation of a flat surface with ultrashort laser pulses at intensity above a threshold value, we induce in the illuminated area a high degree of instability and pattern formation sets in. From linear stability analysis of (1.14), describing the

time profile evolution of irradiated surface, we expect the instability for the "ripple formation" with the wavelength

$$\Lambda_i = 2\pi\sqrt{\frac{2K}{|v_i|}}, \tag{1.24}$$

where K is the specific surface self-diffusion coefficient, v_i are the tension coefficients in (1.14) and i refers to the direction (x or y) with the largest v_i. Assuming the proportionality of v_i to the incident laser fluence F (1.15), we obtain that the ripple wavelength Λ depends only on the laser energy coupled into the material F and on the specific surface self-diffusion coefficient K:

$$\Lambda \propto \sqrt{\frac{K}{F}}. \tag{1.25}$$

This, on the first sight, confusing relation of the ripple wavelength with the fluence can be explained by taking into account the dependence of the specific self-diffusion coefficient K on the surface temperature T [54]:

$$K \propto \frac{1}{k_B T}\exp\left(-\frac{E_a}{k_B T}\right), \tag{1.26}$$

where E_a is the activation energy for surface self-diffusion. Assuming a linear dependence of the surface temperature T with the laser fluence F [63] and taking into account an exponential increase of the thermal surface diffusion K with the surface temperature T (1.26), we obtain exponential growth of the ripples wavelength with T.

1.2.7 Time Evolution

As it has been shown in Sect. 1.2.4, we can analyze the time evolution of the numerically generated pattern taking in account existence of the characteristic time t_c that separates linear and nonlinear regimes.

For a simulation-time much smaller than t_c we observe some periodical surface modifications (Fig. 1.18a), but the pattern has not completely developed yet. By increasing the time up to $t_c/2$ a refined surface pattern consisting of well expressed parallel lines with numerous bifurcations is observed (Fig. 1.18b, cf. also Fig. 1.17). At the time about crossover time t_c, as illustrated in Fig. 1.18c, we notice a coarsening of the ripples. Whereas Fig. 1.18a–c exhibit a progressive development of surface patterns, for times considerably above t_c (Fig. 1.18d) structures start to collapse and kinetic roughening takes place, known from nonlinear dynamics. Though in the

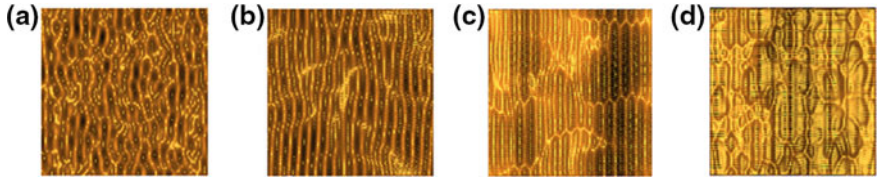

Fig. 1.18 Time evolution of numerically calculated surfaces ($64\pi \times 64\pi$) for $\Pi = 1$ and $\phi = 0$: **a** $t \ll t_c$; **b** $t = t_c/2$; **c** $t = t_c$; **d** $t = 2t_c$ (t_c = 1,600 a.u.)

model the situation is simplified and we did not investigate the pulse-to-pulse development of ripples, the numerical results show that a progressive evolution of structures occurs only in an appropriate time interval.

The effect of multipulse irradiation as well as an important role of feedback effect in ripples formation process have been established in numerous experiments. Figure 1.19 presents in more detail the time (resp. pulse-to-pulse) evolution of the central region of an ablation spot on a Si surface, produced by linearly polarized irradiation at intensity of about 2.6 TW/cm^2. With an increasing number of incident pulses up to 5,000 (Fig. 1.19a–c) the patterns become bigger and complex. This pattern coarsening effect is, again, in agreement with the simulation (Fig. 1.18a–c). At further increase of irradiation dose (Fig. 1.19d), after 10,000 pulses, we detect a collapsing of the structured region (similar to Fig. 1.18d) and the development of the deep crater with linear pattering of the walls, correlated to the direction of laser polarization.

The time evolution in experimental and numerical results allows to establish such general properties as the existence of a certain time interval for successful pattern development and the important role of feedback effect in the ripple formation process.

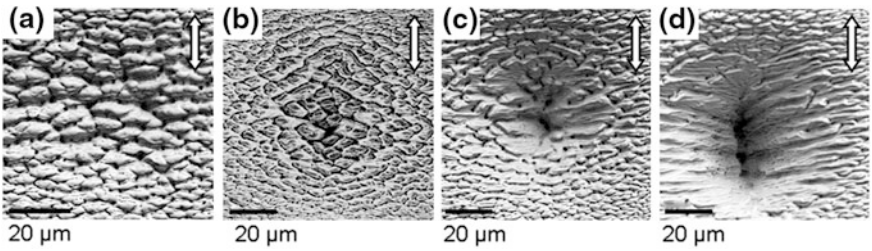

Fig. 1.19 SEM micrographs of pulse-to-pulse evolution of surface patterns at central part of ablated crater on Si by irradiation with linear polarized laser beam of intensity 2.6 TW/cm^2. **a** 1,000 pulses; **b** 3,000 pulses; and **c** 5,000 pulses; **d** 10,000 pulses. *Double arrows* indicate the direction of laser electrical field

1.3 Conclusion

The model for self-organized surface pattern formation upon femtosecond laser ablation was developed by introducing of a dependence on laser polarization. Sigmund's stochastical theory of sputtering and the model of ion-induced surface pattern formation were applied to the investigation of polarization dependent nanostructures. In this approach the laser electric field causes an asymmetry of the initial electron kinetic energy distribution and the related variation in excitation transfer probability. Polarization breaks the symmetry in electron energy transfer and aligns the surface patterns corresponding to the main direction of the energy flow.

Numerically calculated patterns are in good qualitative agreement with experiment for corresponding conditions of orientation and degree of ellipticity of the laser polarization as well as interaction times/number of incident pulses. Moreover, in the framework of this model we have quantitatively estimated the relative influence of input energy on the ripple period that make possible to minimize the size of ripples, selecting suitable parameters of a target material and laser irradiation.

Here it is necessary to note, that our explanation of anisotropic excitation upon femtosecond laser ablation is linked to asymmetric electron energy transfer as one of possible scenario. The microscopic nature of this phenomenon can be more complex and include other processes that break symmetry in the energy transfer and result in a similar effect.

References

1. M. Birnbaum, J. Appl. Phys. **36**, 3688 (1965)
2. D.C. Emmony, R.P. Howson, L.J. Willis, Appl. Phys. Lett. **23**, 598 (1973)
3. J.F. Young, J.E. Sipe, J.S. Preston, H.M. van Driel, Appl. Phys. Lett. **41**, 261 (1982)
4. J.F. Young, J.S. Preston, H.M. van Driel, J.E. Sipe, Phys. Rev. B **27**, 1155 (1983)
5. H. Varel, M. Wähmer, A. Rosenfeld, D. Ashkenasi, E.E.B. Campbell, Appl. Surf. Sci. **127–129**, 128 (1998)
6. A.M. Ozkan, A.P. Malshe, T.A. Railkar, W.D. Brown, M.D. Shirk, P.A. Molian, Appl. Phys. Lett. **75**, 3716 (1999)
7. J. Bonse, H. Sturm, D. Schmidt, W. Kautek, Appl. Phys. A **71**, 657 (2000)
8. M. Henyk, D. Wolffframm, J. Reif, Appl. Surf. Sci. **168**, 263 (2000)
9. J. Bonse, S. Baudach, J. Krüger, W. Kautek, M. Lenzner, Appl. Phys. A **74**, 19 (2002)
10. F. Costache, M. Henyk, J. Reif, Appl. Surf. Sci. **186**, 352 (2002)
11. F. Costache, M. Henyk, J. Reif, Appl. Surf. Sci. **208–209**, 486 (2003)
12. J. Bonse, K.-W. Brzezinka, A.J. Meixner, Appl. Surf. Sci. **221**, 215 (2004)
13. F. Costache, S. Kouteva-Arguirova, J. Reif, Solid State Phenom. **95–96**, 635 (2004)
14. G. Miyaji, K. Miyazaki, Appl. Phys. Lett. **89**, 191902 (2006)
15. G. Miyaji, K. Miyazaki, Appl. Phys. Lett. **91**, 123102 (2007)
16. G. Seifert, M. Kaempfe, F. Syrowatka, C. Harnagea, D. Hesse, H. Graener, Appl. Phys. A **81**, 799 (2005)
17. T. Tomita, K. Kinoshita, S. Matsuo, S. Hashimot, Appl. Phys. Lett. **90**, 153115 (2007)
18. G. Miyaji, K. Miyazaki, Opt. Express **16**, 16265 (2008)

19. J. Bonse, A. Rosenfeld, J. Krüger, J. Appl. Phys. **106**, 104910 (2009)
20. D. Dufft, A. Rosenfeld, S.K. Das, R. Grunwald, J. Bonse, J. Appl. Phys. **105**, 34908 (2009)
21. Z. Li, H. Li, J. Zhang, S. Chen, M. Huang, X. Yu, Opt. Laser Technol. **44**, 923 (2012)
22. J. Reif, Ch. 6 in *Laser Processing of Materials*, ed. by P. Schaaf (Springer, Heidelberg, 2010), p. 113
23. J. Reif, O. Varlamova, M. Ratzke, M. Schade, H.S. Leipner, T. Arguirov, Appl. Phys. A **101**, 361 (2010)
24. J. Reif, F. Costache, M. Henyk, S.V. Pandelov, Appl. Surf. Sci. **197–198**, 891 (2002)
25. O. Varlamova, F. Costache, M. Ratzke, J. Reif, Appl. Surf. Sci. **253**, 7932 (2007)
26. J. Reif, F. Costache, O. Varlamova, G. Jia, M. Ratzke, Phys. Status Solidi C **6**, 681 (2009)
27. S. Höhm, A. Rosenfeld, J. Krüger, J. Bonse, J. Appl. Phys. **112**, 014901 (2012)
28. J. Reif, O. Varlamova, F. Costache, Appl. Phys. A **92**, 1019 (2008)
29. H.M. van Driel, J.E. Sipe, J.F. Young, Phys. Rev. Lett. **49**, 1955 (1982)
30. J.E. Sipe, J.F. Young, J.S. Preston, H.M. van Driel, Phys. Rev. B **27**, 1141 (1983)
31. J.F. Young, J.E. Sipe, H.M. van Driel, Phys. Rev. B **30**, 2001 (1984)
32. M. Henyk, N. Vogel, D. Wolfframm, A. Tempel, J. Reif, Appl. Phys. A **69**, 355 (1999)
33. J. Reif, Opt. Eng. **28**, 1122 (1989)
34. J. Reif, M. Henyk, D. Wolfframm, Proc. SPIE **3933**, 26 (2000)
35. R. Cuerno, A.-L. Barabasi, Phys. Rev. Lett. **74**, 4746 (1995)
36. J. Reif, F. Costache, M. Bestehorn, Ch. 9 in *Recent Advance in Laser Processing of Materials*, ed. by J. Periere, E. Millon, E. Fogarassy (Elsevier, Amsterdam, 2006), p. 275
37. J. Reif, O. Varlamova, S. Varlamov, M. Bestehorn, Appl. Phys. A **104**, 969 (2011)
38. Q. Wu, Y. Ma, R. Fang, Y. Liao, Q. Yu, Appl. Phys. Lett. **82**, 1703 (2003)
39. J. Bonse, M. Munz, H. Sturm, J. Appl. Phys. **97**, 013538 (2005)
40. T.H.R. Crawford, H.K. Haugen, Appl. Surf. Sci. **253**, 4970 (2007)
41. F. Garrelie, J.-P. Colombier, F. Pigeon, S. Tonchev, N. Faure, M. Bounhalli, S. Reynaud, O. Parriaux, Opt. Express **19**, 9035 (2011)
42. J. Erlebacher, M.J. Aziz, E. Chason, M.B. Sinclair, J.A. Floro, Phys. Rev. Lett. **82**, 2330 (1999)
43. E. Chason, T.M. Mayer, B.K. Kellerman, D.T. McIlroy, A.J. Howard, Phys. Rev. Lett. **72**, 3040 (1994)
44. O. Varlamova, M. Ratzke, J. Reif, Solid State Phenom. **156–158**, 535 (2010)
45. C. Misbah, A. Valance, Eur. Phys. J. E **12**, 523 (2003)
46. J.L. Hansen, M. van Hecke, A. Haaning, C. Ellegaard, K.H. Andersen, T. Bohr, T. Sams, Nature **410**, 324 (2001)
47. M.C. Malin, M.H. Carr, G.E. Danielson, M.E. Davies, W.K. Hartmann, A.P. Ingersoll, P.B. James, H. Masursky, A.S. McEwen, L.A. Soderblom, P. Thomas, J. Veverka, M.A. Caplinger, M.A. Ravine, T.A. Soulanille, J.L. Warren, Science **279**, 1681 (1998)
48. C. Teichert, J.C. Bean, M.G. Lagally, Appl. Phys. A **67**, 675 (1998)
49. Y. Kuramoto, T. Tsuzuki, Prog. Theor. Phys. **55**, 356 (1977)
50. G.I. Sivashinsky, Acta Astronaut. **6**, 569 (1979)
51. M. Kardar, G. Parisi, Y.-C. Zhang, Phys. Rev. Lett. **56**, 889 (1986)
52. P. Sigmund, Phys. Rev. **184**, 383 (1969)
53. P. Sigmund, J. Mater. Sci. **8**, 1545 (1973)
54. M.A. Makeev, R. Cuerno, A.-L. Barabasi, Nucl. Instr. Meth. Phys. Res. B **197**, 185 (2002)
55. R.M. Bradley, J.M.E. Harper, J. Vac. Sci. Technol. **6**, 2390 (1988)
56. H.O. Jeschke, M.E. Garcia, M. Lenzner, J. Bonse, J. Krüger, W. Kautek, Appl. Surf. Sci. **197–198**, 839 (2002)
57. A.M. Lindenberg, S. Engemann, K.J. Gaffney, K. Sokolowski-Tinten, J. Larsson, P.B. Hillyard, D.A. Reis, D.M. Fritz, J. Arthur, R.A. Akre, M.J. George, A. Deb, P.H. Bucksbaum, J. Hajdu, D.A. Meyer, M. Nicoul, C. Blome, T.H. Tschentscher, A.L. Cavalieri, R.W. Falcone, S.H. Lee, R. Pahl, J. Rudati, P.H. Fuoss, A.J. Nelson, P. Krejcik, D.P. Siddons, P. Lorazo, J.B. Hastings, Phys. Rev. Lett. **100**, 135502 (2008)

58. J. Reif, Ch. 2 in *Laser-Surface Interactions for New Materials Production. Tailoring Structure and Properties*, ed. by A. Miotello, P.M. Ossi (Springer, Heidelberg, 2010), pp. 19–41
59. J. Reif, F. Costache, S. Eckert, M. Henyk, Appl. Phys. A **79**, 1229 (2004)
60. V. Hertel, R. Stoian, A. Rosenfeld, D. Ashkenasi, E.E.B. Campbell, Riken Rev. **32**, 23 (2001)
61. A. Zangwill, *Physics at Surfaces* (Cambridge University Press, Cambridge, 1988)
62. S. Park, B. Kahng, H. Jeong, A.-L. Barabasi, Phys. Rev. Lett. **83**, 3486 (1999)
63. A. Cavalleri, K. Sokolowski-Tinten, J. Bialkowski, M. Schreiner, D. von der Linde, J. Appl. Phys. **85**, 3301 (1999)

http://www.springer.com/978-3-319-12216-8

Progress in Nonlinear Nano-Optics
Sakabe, S.; Lienau, C.; Grunwald, R. (Eds.)
2015, XXI, 273 p. 137 illus., 44 illus. in color., Hardcover
ISBN: 978-3-319-12216-8